

The orographic impact on patterns of embedded convection during the August 2005 Alpine flood

W. Langhans,^{a*} A. Gohm^b and G. Zängl^c

^a*Institute for Atmospheric and Climate Science, ETH Zurich, Switzerland*

^b*Institute for Meteorology and Geophysics, University of Innsbruck, Austria*

^c*German Weather Service, Offenbach, Germany*

*Correspondence to: W. Langhans, Institute for Atmospheric and Climate Science, ETH Zurich, Universitätstrasse 16, 8092 Zürich, Switzerland. E-mail: wolfgang.langhans@env.ethz.ch

Convective precipitation structures during an Alpine heavy precipitation event in August 2005 are investigated utilising a mesoscale non-hydrostatic numerical model and observational data. The focus is on the mechanisms of convective initiation during the very beginning of the event, when organised cellular updraughts enhanced the precipitation over the southern German Alpine foreland. A set of sensitivity experiments with systematically modified topography is conducted in order to investigate the role of single topographic obstacles in initiating and arranging convection.

A reference simulation proves to be capable of qualitatively reproducing the development of two distinct, flow-parallel aligned, non-stationary, convective precipitation bands, which are observed by radar and surface measurements. The simulations reveal the presence of two low-level convergence lines that provide a primary mechanism for both initiating and aligning convective cells during the analysed period. Mountains embedded in the Alpine foreland are not decisive for triggering and aligning the convective cells in this case, since the primary mechanism provides a consistent forcing for the convective precipitation bands. However, the experiments demonstrate a dependence of the alignment and intensity of one of the precipitation bands upon the position of the pre-existing convergence line relative to a flow-parallel aligned mountain ridge. Enhancement (weakening) of the existing banded structure and convective intensity is achieved if the convergence line is located upstream (downstream) of the ridge with respect to a cross-ridge low-level inflow. The ‘weakening’ mode is characterised by a subsiding cross-ridge inflow into the convergence line that stabilises the atmosphere and therefore inhibits the formation of a continuous convective precipitation band. Copyright © 2011 Royal Meteorological Society

Key Words: precipitation band; orographic precipitation; convergence line; WRF model

Received 8 July 2009; Revised 4 May 2011; Accepted 31 May 2011; Published online in Wiley Online Library 1 August 2011

Citation: Langhans W, Gohm A, Zängl G. 2011. The orographic impact on patterns of embedded convection during the August 2005 Alpine flood. *Q. J. R. Meteorol. Soc.* **137**: 2092–2105. DOI:10.1002/qj.879

1. Introduction

Between midday 21 August 2005 and the afternoon of 23 August 2005, heavy precipitation over Swiss, Austrian, and German Alpine regions led to damaging flooding.

Record-breaking values of accumulated precipitation were obtained over the northern Alpine slopes in central Switzerland during 21 August 2005 and heavy precipitation far beyond the climatological mean occurred during 22 August 2005 over eastern Switzerland and the northern Alpine

flanks in Austria and Germany. A chronological analysis of radar measurements over Switzerland (MeteoSchweiz, 2006a) revealed a shift of the heavy precipitation from Central Switzerland and its adjacent Alpine foreland on 21 August 2005 to the main Alpine crest in eastern Switzerland on 22 August 2005. This displacement of precipitation is in agreement with an eastward propagation of a surface depression, but the spatial distribution of precipitation also changed due to the changing mechanisms of precipitation formation. As mentioned by Zängl (2007c) and shown by Hohenegger *et al.* (2008), embedded convection was triggered in a moist statically unstable environment during the first half of the event, while moist neutrally stratified upslope orographic precipitation has been seen as the dominating mechanism at a later stage of the precipitation event (Zängl, 2007b). Two distinct periods characterised by different precipitation mechanisms have also been reported by Langhans (2008), who detected an enhancement of precipitation by two convective bands over the Alpine foreland during the second half of 21 August 2005, and moist stably stratified flow directed perpendicular to the main Alpine barrier on the evening of 22 August 2005 and later. Clearly, the largest precipitation sums were observed over the central Alpine massif. Still, in this article our interest focuses on the convective activity embedded in the moist flow during the very early stage of the event, since previous studies (e.g. Colle *et al.*, 2008; Kirshbaum and Durran, 2004; Fuhrer and Schär, 2005; Roe, 2005) illustrated the capability of embedded cellular and banded convection to enhance precipitation, and since the predictability of convective precipitation and the physics of its initiation are less consolidated than for stably stratified upslope precipitation.

Previous studies have been devoted to investigations of the atmospheric and topographic conditions necessary for the triggering and formation of banded convection (in contrast to cellular convection). Convective rainbands have been observed frequently, e.g. over the western Kyushu in Japan. Yoshizaki *et al.* (2000) found mesoscale convergence to be one of the main mechanisms for their formation. Convective snowbands initiated downstream of the Rocky Mountains in regions with dry symmetric and inertial instabilities (attributed to a mid-level jet streak) have been studied by Schumacher *et al.* (2010). Cosma *et al.* (2002) indicated the capability of small-scale mountains to form stationary banded convection in lee-side convergence zones. In a more recent study, Kirshbaum and Durran (2005a) simulated banded convective structures during three different shallow convective events over the coastal range in western Oregon. They demonstrated that the presence of roll-like convection is primarily determined by the strength of the vertical wind shear in the unstable cap cloud, but showed that small-scale topographic 'noise' enhances the organised banded structure and intensity of convection.

Further, three-dimensional sensitivity simulations of banded convection over an idealised coastal range revealed that, in contrast to an initiation of convection by random 'noise' in the background temperature field, small-scale topographic features result in more intensive quasi-stationary rain bands (Kirshbaum and Durran, 2005b). Finally, these authors concluded that vertical wind shear and other atmospheric factors are less important for the triggering of banded convection than the formation of lee waves over small-scale hills at the foot of a larger-scale slope. Consistent with these findings, Fuhrer and

Schär (2007) identified the dominating role of indirect triggering of banded convection by gravity wave activity over topographic variations. This aspect has been further analysed by Kirshbaum *et al.* (2007) who identified the importance of the phase of the wave perturbation at the time of saturation at the entrance edge of an orographic cloud. More recently, Godart *et al.* (2009) explored observational data in order to identify a characteristic atmospheric sounding during events with shallow banded convection over the mountainous Cévennes-Vivarais area in France. They concluded that low directional vertical wind-shear, high low-level winds and a sharp decrease of relative humidity with height favour the formation of shallow banded convection.

In this article, the convective bands at the very beginning of the August 2005 heavy precipitation event are analysed using both numerical simulations and observational data. The simulations are compared with rawinsondes, gauge observations, and a radar composite. The aim of the study is to detect the mechanisms of convective initiation and the factors that controlled the banded structure of the convective cells during this period. Furthermore, the impact of topographic features embedded in the low-mountain terrain of the Alpine foreland is depicted. Therefore, numerical experiments with partly removed or flattened orography and others with additional idealised orographic obstacles are performed. The numerical model, the set-up of the sensitivity study, and the available observational data are introduced in section 2. In section 3 operational analyses and observational data are used to describe the large-scale synoptic situation and the characteristic convective precipitation structures. Results of the numerical experiments are presented in section 4 and we summarise our findings in section 5.

2. Method

2.1. Numerical model

The Weather Research and Forecasting (WRF) modelling system is used for numerical simulations. We use version 2.2, in which a time-splitting integration is applied using a third-order Runge–Kutta scheme to solve the non-hydrostatic Euler equations in flux form (Skamarock *et al.*, 2005). The variables are spatially discretised on a staggered Arakawa-C grid and a fifth-order accurate upstream discretisation scheme is applied for their advection. A conservative positive-definite advection scheme has been chosen for moisture variables, since non-positive-definite schemes result in an overestimation of surface precipitation (Skamarock and Weisman, 2009). As suggested by Zängl (2004), explicit horizontal diffusion is calculated in physical space. In the vertical, 39 unevenly spaced σ levels are applied, which correspond to 38 half- σ levels. The lowermost half- σ level is located at $\sigma = 0.997$ (≈ 26 m above ground level). The vertical resolution decreases monotonically with height to $\Delta z \approx 870$ m at the model top (100 hPa). Note that all numerical simulations in this study are performed with a generalised vertical coordinate (Zängl, 2007a), in which the terrain-following σ coordinate levels are gradually transformed to pressure levels with increasing height. Thereby, small-scale topographic structures decay rapidly with height and reduce the numerical error arising from the calculation of the horizontal advection on sloping coordinate surfaces (Zängl, 2007a). Three model domains are used

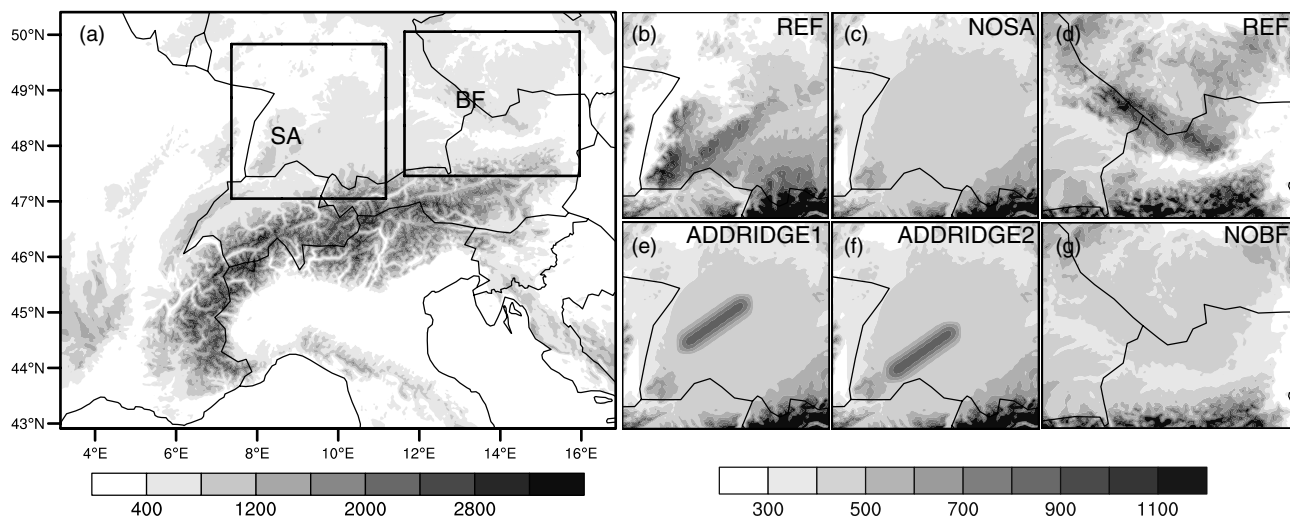


Figure 1. Topography (m above msl) of (a) the inner domain of the REF run showing areas Black Forest (BF) and Swabian Alps (SA), which are modified in the sensitivity experiments. The expansions illustrate the topography of (b, c, e, f) SA and (d, g) BF, as used for the sensitivity runs listed in Table 1.

with horizontal mesh sizes of 30 km, 10 km, and 2 km, respectively; the latter two are each two-way nested into the next coarser one. The innermost domain (Figure 1(a)) roughly covers the Alpine area, i.e. Switzerland, Austria, and the German Alpine foreland. The exact positions of the domains are indicated in Figure 2(a). The initial and boundary conditions are obtained from the European Centre for Medium Range Weather Forecasts (ECMWF) analysis data. The operational analysis data are provided on 16 pressure levels on a $0.25^\circ \times 0.25^\circ$ latitude–longitude grid. A two-way nested reference run is conducted that covers a period of 36 h and is initialised at 0000 UTC on 21 August 2005. The starting time is chosen such as to allow for a spin-up time of 6 h before 0600 UTC (0800 LST; LST=UTC+2 h), when the observation interval of the routinely measured daily accumulated precipitation, which will be used for validation purposes, starts. In domains 1 and 2, subgrid-scale cumulus precipitation is parametrised by the new Kain–Fritsch mass-flux scheme (Kain, 2004). In domain 3, convective precipitation is assumed to be explicitly resolved. Preliminary tests using different horizontal resolutions revealed no significant improvement of the quantitative precipitation forecast with a 1 km grid spacing and a similar precipitation field was produced with a grid spacing of 3 km. The PBL parametrisation is accomplished with the Yonsei University (YSU) scheme (Hong *et al.*, 2006), a non-local first-order scheme that uses a prescribed profile to determine the vertical diffusion coefficients. The long-wave part of the radiation is calculated with the Rapid Radiative Transfer Model (RRTM; Mlawer *et al.*, 1997). A modified Dudhia (1989) short-wave scheme is used that comprises the shading effects of mountains. Land surface processes are modelled by a five-layer thermal diffusion scheme. Microphysics are described by the so-called WRF single-moment bulk microphysics scheme WSM6 (Hong and Lim, 2006), a single-moment scheme with prognostic graupel. The microphysics scheme has influence on the formation of precipitation, and previous simulations of this heavy precipitation event supported the choice for this scheme (Langhans, 2008).

In this article several sensitivity simulations are presented using modified topography. Table 1 summarises the orographic characteristics of all performed numerical

simulations and introduces abbreviations, which will be used in the following. The reference run (REF) uses a 30'' orography truncated to the model grid. The innermost domain is shown in Figure 1(a). The influence of single mountain ridges is explored by the experiments NOBF and NOSA, in which the Bavarian Forest (BF) and the Swabian Alps (SA), respectively, are removed. The modifications of these two subregions are shown in Figures 1(c, g). The ridges are flattened by applying the following weighting function b_{ij} to the REF terrain elevation $H_{R,ij}$ at certain gridpoints (i, j) :

$$H_{ij} = (1 - b_{ij})H_{R,ij} + b_{ij}H_M,$$

$$\text{where } b_{ij} = a_{ij} \exp(1 - a_{ij}),$$

$$\text{and } a_{ij} = \sin\left(\pi \frac{i - i_s}{i_e - i_s}\right) \sin\left(\pi \frac{j - j_s}{j_e - j_s}\right),$$

where i_s , i_e , j_s , and j_e specify the start and end points of the target areas in which the orography is modified (see also boxes in Figure 1(a)). Outside these target areas, b_{ij} is zero. The sine function allows for the increase of weights ($b_{ij} \rightarrow 1$) for points approaching the centre of the target area, which will receive a new mean terrain height H_M of 400 m in NOBF and 420 m in NOSA. The mean terrain height has been chosen to fit the terrain height of the surrounding areas. A fast transition from the real orography to the new mean terrain elevation is ensured by the exponential function. This simple method allows us to gradually adjust the height of a ridge to the new mean terrain elevation. Within the NOALPS run, the terrain elevation in the innermost Alpine domain is simply limited to 500 m, which completely removes the Alpine arc. Idealised ridges are added to the flattened NOSA topography in two further experiments: with respect to the SA, in the ADDRIDGE1 run a new ridge is used slightly further north, whereas in the ADDRIDGE2 simulation a ridge is added right at its original location. Both ridges have been rotated to be parallel to the SA and have similar proportions (Figures 1(e, f)). The additional idealised topography ΔH is formulated as

$$\Delta H_{ij} = \Delta H_{\max} \cos^2\left(\frac{\pi l_{ij}}{2a}\right),$$

Table I. Overview of the conducted numerical simulations and description of the topographic modifications.

Name	Topography
REF	Real (30'').
NOBF	REF without Bavarian Forest (BF).
NOSA	REF without Swabian Alps (SA).
ADDRIDGE1	NOSA with additional elongated ridge in the vicinity of the previous location of SA.
ADDRIDGE2	NOSA with additional elongated ridge at previous location of SA.
NOALPS	No higher than 500 m in domain 3.

with $\Delta H_{\max} = 400$ m, $l_{ij} = \sqrt{(j - j_i)^2 + (i - i_i)^2}$ the distance to the 160 km long centreline of the rotated ridge, and $a = 20$ km the mountain halfwidth.

2.2. Observational data

2.2.1. Rain-gauge networks

For validation purposes, daily accumulated precipitation observed at sites of several institutes are compared against the numerical simulations. The applied datasets are provided by the Austrian Central Institute for Meteorology and Geodynamics (ZAMG), the German Weather Service (DWD), the Swiss Weather Service (MeteoSwiss), and the Austrian Hydrological Service (HZB). The 648 DWD measurement sites cover the German states of Bavaria and Baden-Württemberg, which form the southern part of Germany. The ZAMG data consist of daily measurements at 265 stations. Seventy of the MeteoSwiss rain stations belong to a network of automatic weather stations (ANETZ). At the remaining 425 Swiss stations (NIME) manual daily precipitation measurements are conducted. The HZB provides daily precipitation sums at 783 stations in Austria. Note that data are missing at several of the above-mentioned stations, which reduces the effective station number. In total, the complete southern German and Alpine area is covered by the available observations, except for the southern part of the Alps.

2.2.2. CERAD radar composite

The Central European Weather Radar Network (CERAD) provides radar composites from operational radars in Austria, Germany, Switzerland, Hungary, Croatia, Slovenia, Poland and the Czech Republic. The horizontal resolution of one image pixel is $2 \text{ km} \times 2 \text{ km}$. A detailed description of the CERAD product is given by Randeu *et al.* (1996). The data, provided by ZAMG, consist of half-hourly rain rates, which are subdivided into eight classes. For the comparison with gauge observations and model results, these rain rates are integrated over a 24 h period. The calculation of accumulated precipitation can practically be achieved by the summation of the mean values, the upper limits, or the lower limits of each class. However, the results show a large variability. As a consequence also of other well-known problems

of operational radar measurements*, the CERAD radar composites will not be discussed in a quantitative manner in the remainder of this article. However, the structure and spatial distribution of precipitation estimated by the radar still add valuable information about the prevailing mechanisms of precipitation formation.

3. Synoptic situation and precipitation field

The synoptic situation during this heavy precipitation event is only roughly outlined here, since detailed descriptions can be found in the literature (e.g. MeteoSchweiz, 2006a; Zängl, 2007b,c; Hohenegger *et al.*, 2008). An analysis of the accumulated precipitation field in the Alpine region and a climatological classification of this extreme event is presented also by MeteoSchweiz (2006b). On 20 August an upper-level trough began to cut off over France. Embedded in the eastward progressing system it passed the Alps on its south side and deepened until 22 August (MeteoSchweiz, 2006a). Figure 2 illustrates the synoptic situation, as analysed by the ECMWF, for the beginning of the event at 1200 UTC on 21 August 2005. The distribution of the geopotential height at 300 hPa (Figure 2(a)) shows a cut-off low located to the south of the Alps. Associated with the upper-level trough was a surface depression with its occluded frontal system (not shown). The surface low over the Gulf of Genoa carried Mediterranean air counterclockwise around the Alps and finally formed a strong low-level jet directed towards the northern Alpine slopes (Figure 2(b)). The wind was directed nearly parallel to the Alps during this period, and large amounts of moisture were transported towards the northern Alpine slopes. Figure 2(a) shows relative humidities that are in general higher than 95% along the northern Alpine rim at 1200 UTC on 21 August 2005, especially in Switzerland. The corresponding moisture flux along the northern Alps at the 850 hPa level (Figure 2(b)) reveals peak values of more than $0.12 \text{ kg m}^{-2} \text{ s}^{-1}$ upstream of Switzerland.

Figure 3(a) shows the daily accumulated precipitation measured from the rain gauges between 0600 UTC on 21 August and 0600 UTC on 22 August 2005. Highest amounts of precipitation were recorded in central Switzerland. There, a large area was affected by more than 90 mm of precipitation, and at some Swiss stations more than 120 mm of precipitation were measured (e.g. Stans 135 mm, Sangernboden 121 mm, Napf 127 mm, Kurzenalp 123 mm). The maximum daily precipitation occurred in Wasen im Emmental with 170.7 mm. Significantly less precipitation fell over southern parts of Switzerland, resulting in a distinct north–south precipitation gradient. Apart from the precipitation maximum in central Switzerland, secondary, less intensive, precipitation maxima can be identified over northern parts of Switzerland and southern Germany. Two preferred areas of increased precipitation can be identified (A and B in Figure 3(a)), which are elongated from northeast to southwest in a banded manner. Along the SA precipitation was higher than in surrounding regions and the other banded region extended from the BF westwards. The one to the north produced slightly more rain (>75 mm) than the southern one, and the precipitation bands are clearly distinguishable

*Processes that affect the quality of rain measurements by radars are e.g. ground cluttering, partial or total beam blocking in complex orographic areas, radar calibration, proper Z–R relation, and evaporation of rain.

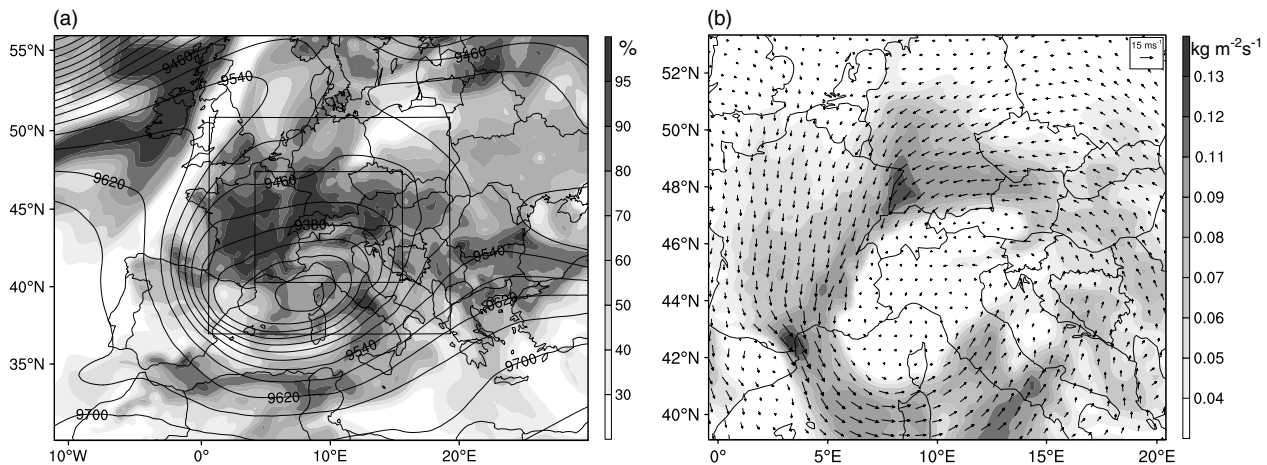


Figure 2. ECMWF analysis fields at 1200 UTC on 21 August 2005: (a) 300 hPa geopotential height (solid lines at 40 gpm intervals) and 850 hPa relative humidity (grey shading, %) in domain 1 and (b) 850 hPa moisture flux (grey shading, $\text{kg m}^{-2}\text{s}^{-1}$) and wind vectors in domain 2. Boxes in (a) indicate the position of the nested domains.

by a relative minimum of precipitation between them. Figure 3(b) shows the daily precipitation from the radar measurements calculated by the summation of the lower limits of the rain-rate bins. The radars capture the precipitation maximum over Switzerland and confirm the presence of both convective precipitation bands. Obviously, the intensity of the convective precipitation in both bands is drastically overestimated and also the strong signals over the northeast of the SA are not confirmed by the surface measurements (Figure 3(a)). In the remainder of this article, the northern band will be denoted as band A, the southern one as band B (also Figure 3(a)). These features give rise to the assumption that convective precipitation bands increased the rainfall already upstream of the main Alpine rim and caused large spatial precipitation gradients. Note also that the northern band in Figure 3(b) appears to be interrupted to the lee of the BF, where very weak signals are obtained. Moderate precipitation at the eastern edge of the Alps is also recognisable and indicates the orographic lifting of the northwestward-moving air mass.

For a more detailed analysis of the evolution of precipitation during the beginning of the event, hourly rain rates measured by the operational CERAD radars are shown for the northern Alps in Figure 4. At 1440 UTC (Figure 4(a)) a precipitation band is visible to the west (downstream) of the BF. Scattered precipitation echoes are obtained east (upstream) of the BF as well. One hour later (Figure 4(c)) two bands are recorded to the west of the BF. Then at 1641 UTC and 1738 UTC (Figure 4(e, g)) band A is positioned over the SA and band B is located slightly further to the south and again seems to trail behind the BF. The observed banded shape of the precipitation structures agrees with the above discussed results from the rain-gauge measurements, which showed a clear separation between two regions with high precipitation sums.

4. Results

4.1. Evaluation of the reference run

Observed and predicted vertical atmospheric profiles at Munich (Figure 3(c)) at 1200 UTC on 21 August 2005 are shown in Figure 5. Profiles from the ECMWF analysis have been added to the figures, in order to allow for a quantitative

comparison between the REF run and its driving model. The following results from WRF have all been obtained on the innermost model grid. Figure 5(a) indicates a maximum observed wind speed of 17 m s^{-1} at 3.5 km above mean sea level (amsl), which is reproduced quite well by the REF run. In agreement with the observation, the ECMWF analysis and the REF run reveal a continuous easterly wind above 1 km amsl (Figure 5(b)). Discrepancies occur close to the surface, where the observed winds turn to north. A low-level shear layer of $\sim 80^\circ \text{ km}^{-1}$ and unidirectional shear above was also observed and modelled at Stuttgart (not shown), which is located $\sim 50 \text{ km}$ north of SA (Figure 3(c)).

The decrease of the saturation equivalent potential temperature θ_{es} (Figure 5(c)) indicates a conditionally unstable stratified atmosphere. Parcels ascending adiabatically from the ground would experience positive buoyancy at $\sim 1\text{--}2 \text{ km}$ amsl. The equilibrium level (LNB) is reached at roughly 7 km amsl in REF compared to an observed LNB at $\sim 5.5 \text{ km}$ amsl. Moist instability is also indicated by a 3 km deep layer with negative values of the squared moist Brunt–Väisälä frequency (not shown). The vertical structure of the simulated equivalent potential temperature θ_e agrees with the observed sounding, but the model has higher θ_e within the planetary boundary layer (PBL). A maximum deviation of 3 K is reached near the ground and results from an overestimation of the temperature. Note that the observed profile in Figure 5(c) runs between the ECMWF analysis (with too low θ_e values close to the surface) and the REF run. The vertical distribution of humidity (Figure 5(d)) is characterised by a rapid decrease from saturated conditions below 1.5 km amsl to 80% relative humidity at 3 km amsl. The thermodynamic profile reveals the same features as the mean profile found by Godart *et al.* (2009) from 36 shallow banded convective events. In contrast to their mean profile, the relative humidity increases to almost 90% between 3 and 5 km amsl and the near-surface θ_e is larger. Similar moisture and temperature profiles are retrieved for Stuttgart. However, again due to slightly too high temperatures in the REF run, the near-surface profile of θ_e in Stuttgart is not captured accurately inside the PBL. It should be mentioned that simulations with different PBL parametrisations did not result in better agreement.

In a next step, the development of convective precipitation patterns produced by the REF run is compared to the

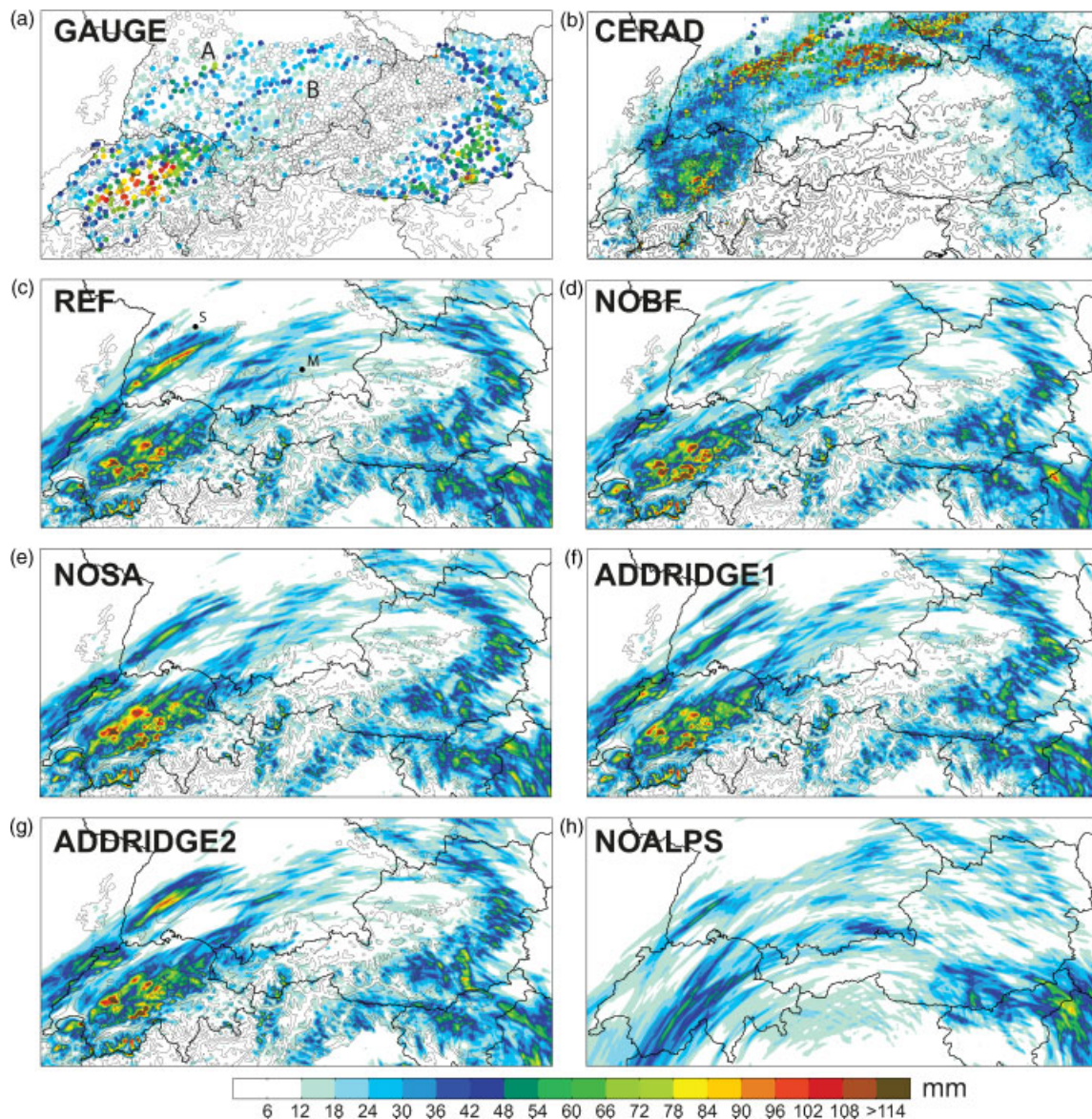


Figure 3. Accumulated total precipitation (mm) obtained between 0600 UTC on 21 August 2005 and 0600 UTC on 22 August 2005 from (a) the rain-gauge measurements (GAUGE), (b) the CERAD radar composite, and the numerical simulations (c) REF, (d) NOBF, (e) NOSA, (f) ADDRIDGE1, (g) ADDRIDGE2, and (h) NOALPS. Rain gauges with precipitation records of less than 12 mm are indicated by black circles in (a). Topography is indicated by contours at 1000 m intervals. Labels A and B indicate the positions of the precipitation bands, and S and M the locations of Stuttgart and Munich, respectively.

observed precipitation. Modelled rain rates are shown together with the above described radar rain rates in Figure 4. The REF rain rates have been estimated from half-hourly rain totals, since instantaneous rain rates were not available. In principle the REF run captures the observed development of the convective precipitation structures, as two distinct convective bands are initiated over southern Germany. However, discrepancies occur in the timing and the exact location of the bands. In contrast to the simulation, the observed band A appears further to the north, close to the BF at 1440 UTC. In its close vicinity the triggering of band B is observed at 1540 UTC. Later at 1641 UTC the observed band A propagates westward and is then located above the SA. In the REF simulation only band B is initially triggered at the location of the BF, while precipitation band A is already located over the SA at 1430 UTC (Figure 4(b)). Still, at 1530 UTC the location of band B (Figure 4(d)) agrees very well with the observed band B and also the position of

the northern band A does reveal some qualitative agreement with the radar measurements after 1630 UTC (Figure 4(f, h)).

The predicted accumulated precipitation field of the REF simulation is shown in Figure 3(c). Compared to observations (Figure 3(a)), the REF simulation shows good skill in capturing the spatial precipitation distribution. Orographic precipitation over the eastern end of the Alpine ridge is generated and both location and amount agree very well. In agreement with the observations, the maximum amount of precipitation accumulates in Central Switzerland. The simulation reproduces the observed precipitation amount of more than 80 mm over the Swiss Jura mountains. Pronounced banded structures appear over the Alpine foreland in southern Germany, which were observed both by the radar (Figure 3(b)) and the rain-gauge measurements (Figure 3(a)). Convective band A is overestimated by ~ 20 mm in comparison with the rain-gauge measurements. This could result from the above-mentioned too early onset of precipitation over the SA

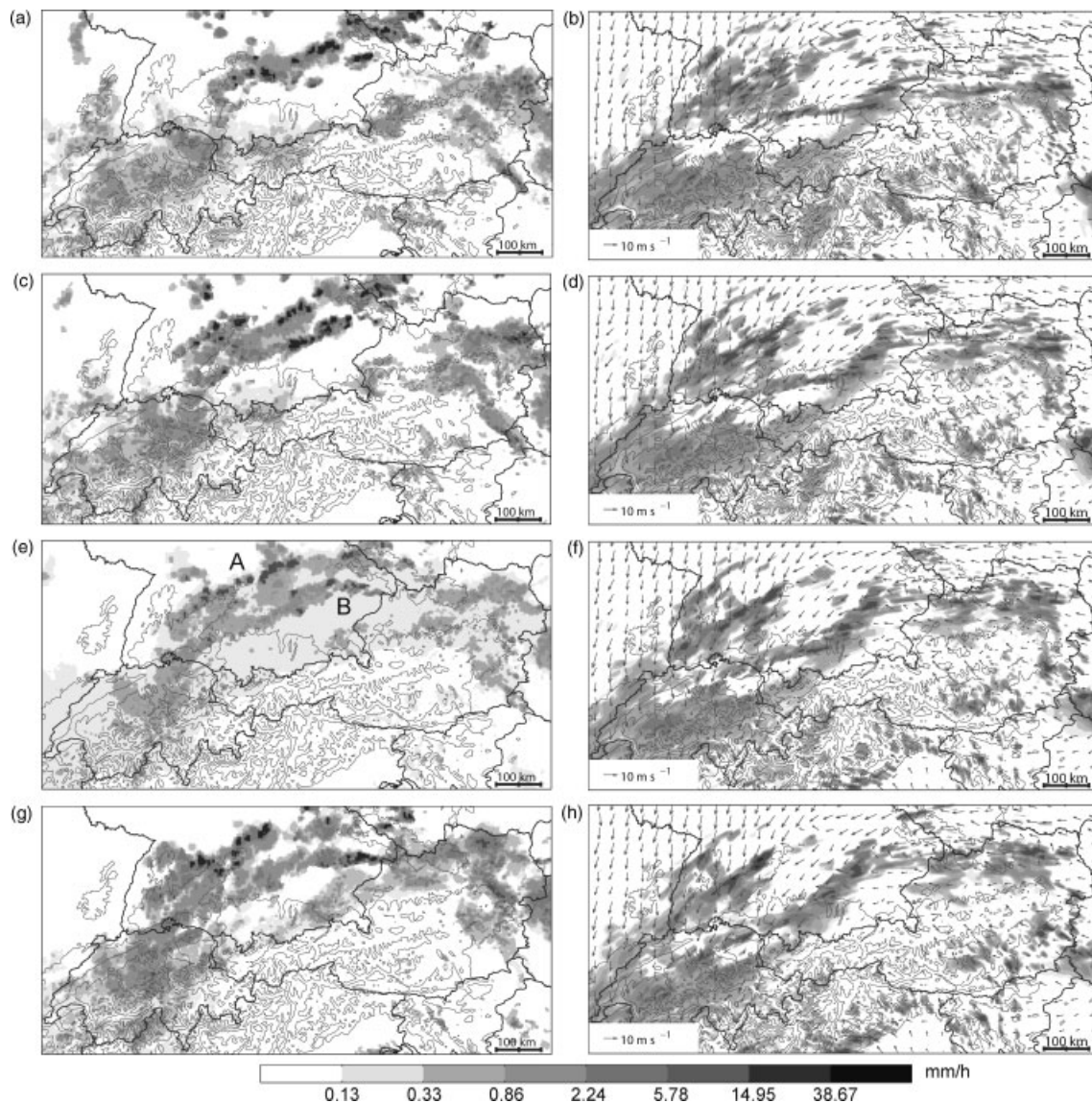


Figure 4. Rain rates (mm h^{-1}) obtained from (a, c, e, g) the CERAD product at (a) 1440 UTC, (c) 1540 UTC, (e) 1641 UTC, and (g) 1738 UTC on 21 August 2005 and from (b, d, f, h) precipitation totals of the REF simulation for half-hourly periods (converted to mm h^{-1}) starting at (b) 1430 UTC, (d) 1530 UTC, (f) 1630 UTC, and (h) 1730 UTC on 21 August 2005. Also shown are velocity vectors from REF on the first model level ($\approx 26 \text{ m agl}$). Topography is indicated by contours at 1000 m intervals.

(Figure 4(b)). However, the minimum of precipitation between the two most pronounced bands is well captured. The origin of precipitation band B in the east of Germany is collocated with the position recorded by the radar.

Further evaluation of the REF simulation shows that the convective bands are in phase with two low-level convergence lines. Figure 6(a) shows the convergence of the near-surface horizontal wind and total precipitation hydrometeor mixing ratio at 1.2 km amsl and at 1630 UTC on 21 August. Precipitation occurs near regions with increased low-level convergence. The convergence exceeds $80 \times 10^{-5} \text{ s}^{-1}$ to the northwest of the SA and downstream of the BF. At the latter location the flow seems to be modified by either a channelling of the flow in the Danube valley (located between the northern Alpine rim and the BF) or by the BF itself. Furthermore, Figure 6(a) reveals that the triggered bands are not continuous ‘roll-like’ bands (as detected by Kirshbaum and Durran, 2005a), but are composed of multiple single cellular updraughts. Short banded convective patterns are only produced in

regions where the convergence lines are continuously strong. From this analysis, we conclude that the presence of the convergence lines seems to be the driving mechanism for triggering the convective cells and aligning them in a banded manner. The orographic impact on both the convergence zones and the convective patterns is clarified in the following sensitivity study.

4.2. Topographic effects

4.2.1. Bavarian Forest

The daily accumulated precipitation on 21 August simulated by the NOBF run (Figure 3(d)) reveals highest precipitation peaks over central Switzerland and the Swiss Jura. Similar to the REF run, precipitation bands appear over the SA and southeastern Germany. However, the intensity of band A over the SA region is reduced by more than 40 mm. In contrast to the REF run, which generated less precipitation over the leeward slopes of the BF than over the

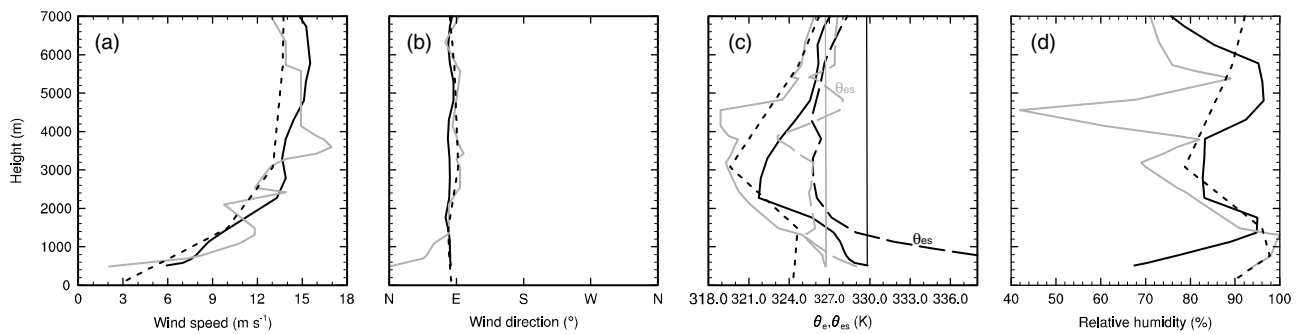


Figure 5. Vertical profiles from the REF simulation (solid black), radio sounding (grey), and ECMWF analysis (short-dashed black) at Munich at 1200 UTC on 21 August 2005: (a) wind speed (m s^{-1}), (b) wind direction ($^{\circ}$), (c) equivalent potential temperature (K), and (d) relative humidity (%). The location of Munich is indicated in Figure 3(c). Also shown in (c) are saturation equivalent potential temperatures θ_{es} (long-dashed) from observation and REF; thin lines in (c) indicate adiabatic ascent from the surface.

windward slopes (Figure 3(c)), the NOBF run smoothes this west–east precipitation gradient and thereby increases the precipitation at the former leeside slopes by roughly 12 mm. Figure 6(b) shows the near-surface convergence and total precipitation mixing ratio at 1.2 km amsl for the NOBF run at 1630 UTC on 21 August 2005. Convective cells are triggered in two lines with strong convergence over southern Germany, whereby the locations of both bands A and B appear to be slightly modified compared with the REF run (Figure 6(a)). Astonishingly, the location of precipitation band A is modified relatively strongly at this time and the convergence line appears to be less continuous than in the REF run. The length of band A appears to be significantly reduced, since it is split into part A2 to the northwest of the SA and part A1 further south (Figure 6(b)). Analysis of the period between 1000 and 1200 UTC on 21 August, when the convergence line responsible for triggering convection in band A is approaching the BF, shows modifications of the low-level convergence line in the REF run as a result of mountain-induced flow deflections. Figure 7(a) shows that cells are triggered in the westward-propagating line already upstream of the BF in REF (and in NOBF, Figure 7(b)), but also downstream of the northwestern tip of the BF, where winds are converging due to weak flow around the BF. The leeward convergence in the REF run (Figure 7(a)) contributes to a seemingly faster westward propagation of the convergence line. Such mountain flow-related modifications of the convergence line are clearly not simulated in the NOBF simulation and convective cells are not triggered downstream (to the west) of the BF in the NOBF run (Figure 7(b)). As a consequence, the convergence line in the NOBF run is located slightly further to the east after crossing the BF and is partially positioned southeast of the SA around 1600 UTC, instead of establishing completely over the northwestern flanks of the SA as in the REF simulation (also Figures 6(a, b)).

In terms of its structural development, precipitation band A is revealed to be sensitive to a removal of the BF, because the exact position of the convergence line in relation to the SA seems to determine the intensity of band A. Although the BF appears not to be the governing factor for controlling the position of the convergence lines, it deflects the low-level flow and causes convergence downstream of the BF, which favours the triggering of convection (as described by Cosma *et al.*, 2002). We found mountain Froude numbers

$Fr > 2^{\dagger}$ for the flow over the BF, such that the leeside convergence appears not to result from low-Froude-number flow behaviour (e.g. flow splitting). Here, Froude numbers are also considerably larger than those prescribed in the experiments of Cosma *et al.* (2002) ($Fr = 0.62$). Further, the release of condensational latent heat is expected to increase the upslope lift (Schneidereit and Schär, 2000; Rotunno and Ferretti, 2001), shift the onset of nonlinear effects (e.g. flow stagnation and reversal) to smaller critical Froude numbers (Jiang, 2003; Colle, 2004), and decrease the amplitude of lee waves (Durran and Klemp, 1983). We did not detect any gravity-wave patterns over the leeslopes of the BF and can therefore exclude the triggering by wave-induced lifting (as described by Kirshbaum *et al.*, 2007). The most plausible explanation for the leeside convergence appears to be the flow over heated terrain, which results in convergence and lifting in the lee, although the orographic response (without heating) would produce downward motion in the lee (Crook and Tucker, 2005; Tucker and Crook, 2005). A 200–300 m deep superadiabatic near-surface layer (not shown) gives evidence for this diabatic heating over the BF.

4.2.2. Swabian Alps

Figure 3(e) shows the accumulated precipitation field on 21 August 2005 for the NOSA simulation. The maximum precipitation over the SA is smaller than in the REF run, but the location of band A remains relatively unaffected, which is due to the fact that the location of the convergence line is unaffected (Figure 6(c)). Less precipitation is generated over the northern BF region, which has been removed here as well.

Figures 8 and 9 show vertical cross-sections perpendicular to the SA from northwest to southeast. The position of the section is indicated in Figure 6(a). The plotted parameters are averaged over a distance of 60 km into the cross-section. Figure 8 shows the convective inhibition (CIN), convective available potential energy (CAPE), and the vertical velocity, and Figure 9 shows the equivalent potential temperature θ_e , convergence of the horizontal wind, and the mixing ratios of rain, cloud water, and graupel. Distributions of CAPE and CIN have been diagnosed based on the lifting of a parcel starting from each grid point. Figures 8(b)

[†]Three-dimensional fields of the Froude number $Fr = U/(h_m N)$ have been estimated from the cross-BF wind speed U , a mountain height $h_m = 500$ m, and the Brunt–Väisälä frequency N .

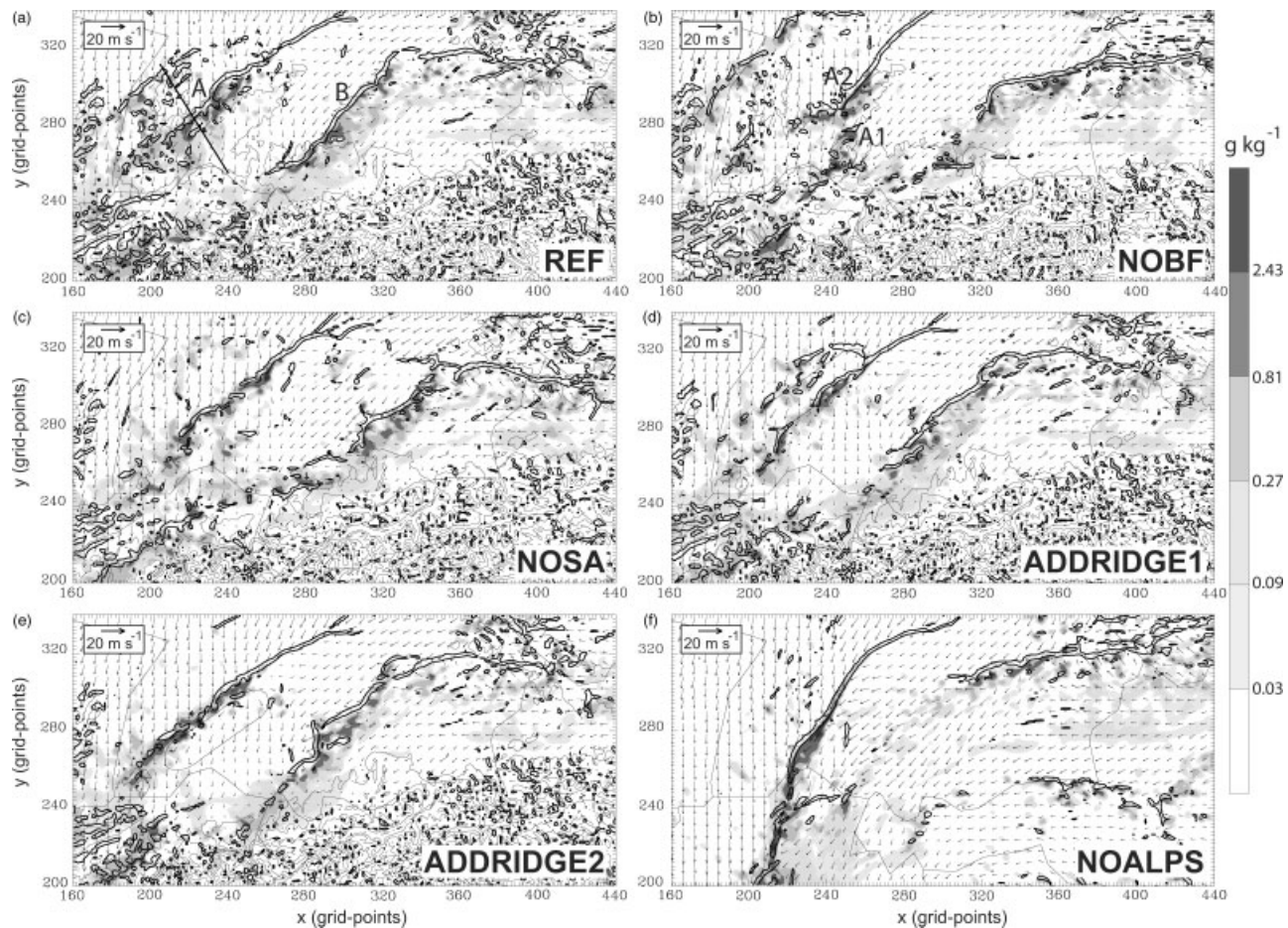


Figure 6. Total precipitation hydrometeor mixing ratio at 1.2 km amsl (shaded contours, g kg^{-1}), convergence of the horizontal wind (thick black contour, $80 \times 10^{-5} \text{ s}^{-1}$) and wind vectors on the lowest model level at 1630 UTC on 21 August 2005 from simulations (a) REF, (b) NOBF, (c) NOSA, (d) ADDRIDGE1, (e) ADDRIDGE2, and (f) NOALPS. Topography is indicated by thin black contours every 600 m.

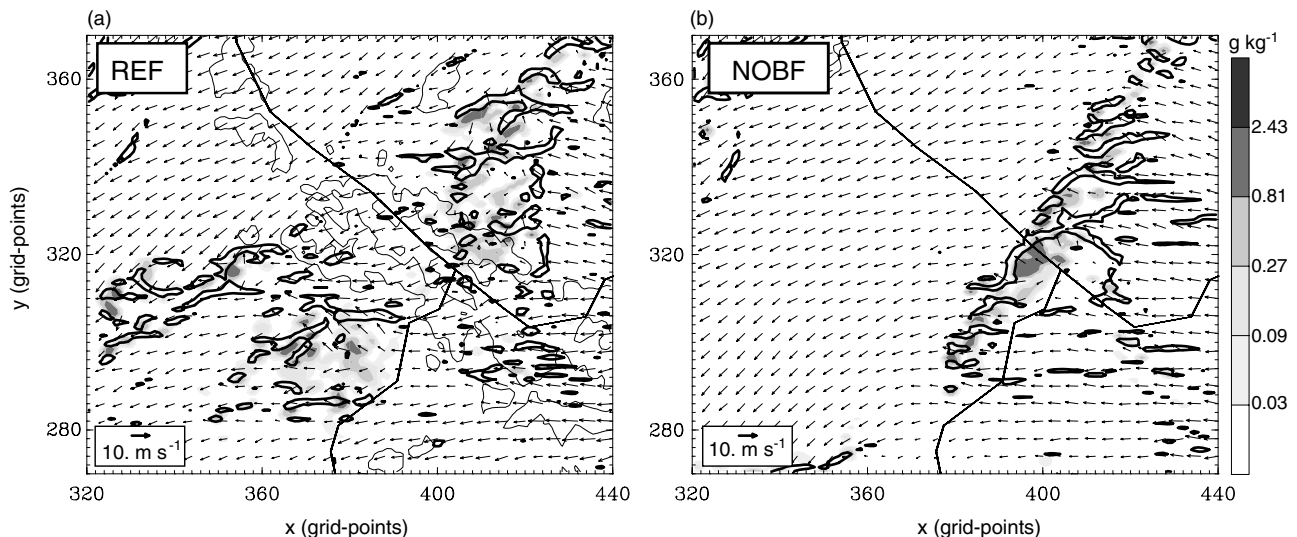


Figure 7. As Figure 6, but for the vicinity of BF at 1100 UTC on 21 August 2005 from (a) REF and (b) NOBF. Topography is indicated by grey contours every 300 m.

and 9(b) confirm that at 1630 UTC on 21 August 2005 convective updraughts are mostly triggered in a sharply defined region of convergence. The average vertical velocity exceeds 1.2 m s^{-1} above the convergence zone, which is similar to the magnitude in the REF run (Figure 8(a)). Convective precipitation to the northwest of the convergence line is prevented by relatively large values of CIN, which

reach up to 1 km amsl (Figure 8(b)). In contrast, the REF simulation reveals orographically triggered convective cells at the northwestern flanks of the BF (Figure 9(a)). The inversion of θ_e is about 8 K in both the REF and NOSA simulations, at least to the northwest of the convergence line. Detailed analysis showed that the horizontal gradients of CIN, CAPE, and θ_e (Figures 8(a–d) and 9(a–d)) result

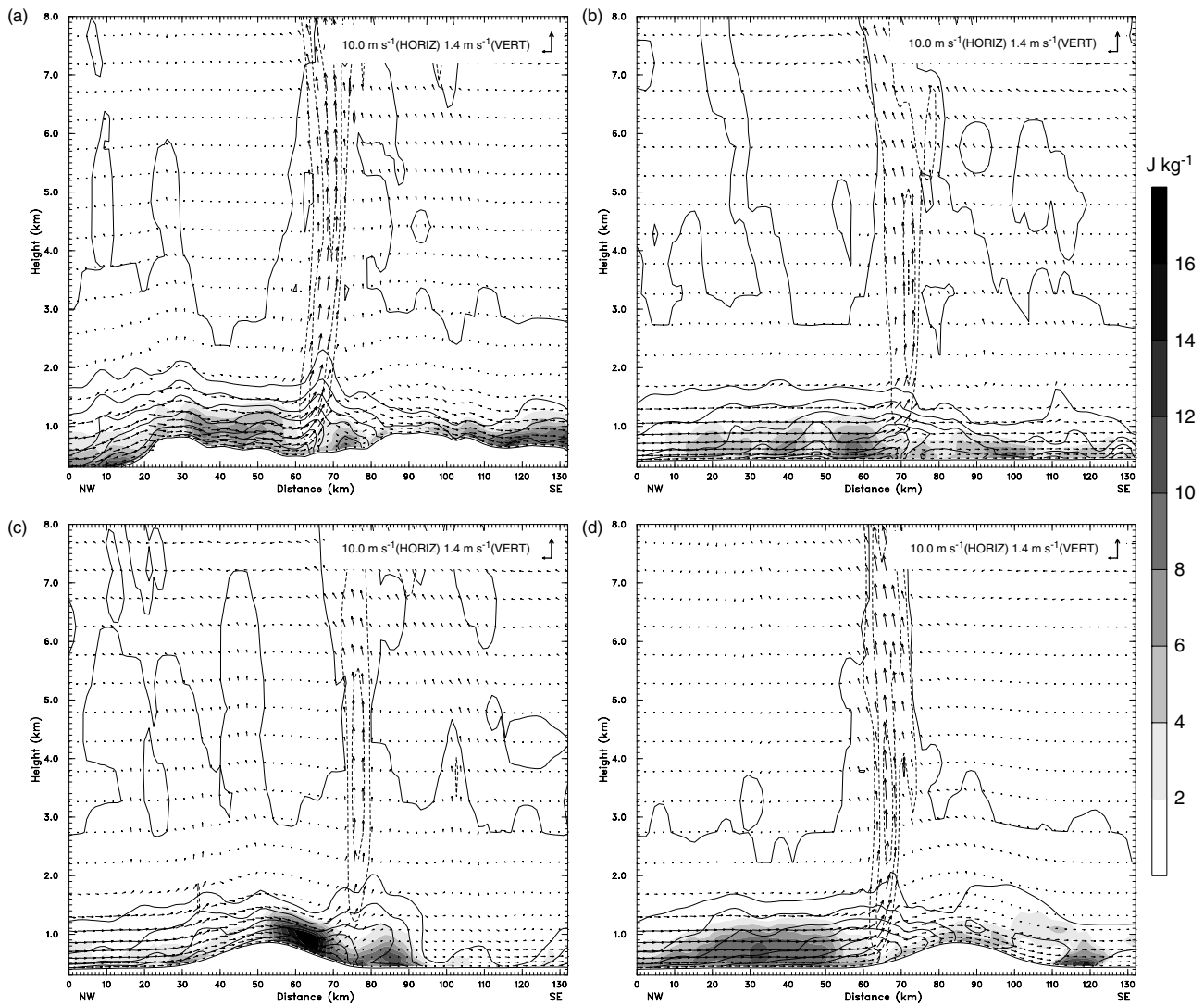


Figure 8. Vertical cross-section of CIN (shading, J kg^{-1}), CAPE (black solid contours with 50 J kg^{-1} increments; the uppermost thick solid line is the zero contour), vertical velocity (black dashed contours with 0.4 m s^{-1} increments, no zero contour) and plain-parallel wind vectors at 1630 UTC on 21 August 2005 from simulations (a) REF, (b) NOSA, (c) ADDRIDGE1, and (d) ADDRIDGE2. Parameters are averaged over a distance of $\sim 60 \text{ km}$ into the cross-section, 30 km in each direction. The location of the section is indicated in Figure 6(a).

from triggering of embedded convection upstream of the SA region (e.g. Figure 7(a)). This results in a removal of low-level convective potential from the airmass, which is advected to the region southeast of the SA in the following. The air to the north and upstream of the SA exhibits significantly less embedded convective activity. It is found that this airmass difference, which is uniform along the convergence line, had been strengthened also after the establishment of the convective band.

The graupel amounts and the vertical extent of the convective updraught (Figures 8(a–d) and 9(a–d)) indicate the initiation of deep convection in the convergence zone. The simulation demonstrates that removing the SA does not affect the position of the convergence line. However, in comparison to the REF run the amount of accumulated precipitation in band A is significantly decreased.

4.2.3. Additional idealised ridge 1

The results from the ADDRIDGE1 run, in which an idealised ridge has been added 40 km to the north of the SA are described in the following. In comparison to both the

REF and NOSA runs, the daily accumulated precipitation field in ADDRIDGE1 (Figure 3(f)) shows a decrease of the intensity of precipitation band A. A secondary maximum is produced over the northwestern flank of the idealised ridge, where (in contrast to NOSA) cells are triggered (Figure 9(c)). The position of the low-level convergence line at 1630 UTC on 21 August 2005 is unaffected and remains unmodified compared to REF and NOSA, which in this simulation is slightly to the southeast of the new idealised ridge (Figure 6(d)).

However, the intensity and continuity of the convective band are modified by the presence of the ridge. The band of convective cells in Figure 6(d) appears to be less uniform than in REF and NOSA, since an area with relatively low precipitating hydrometeor content and lower values of convergence forms a discontinuity in the banded convective structure. At the same time both the NOSA and REF simulations show a more continuous convergence line over southwestern Germany. The vertical cross-section in Figure 8(c) shows very large values of CIN ($\sim 20 \text{ J kg}^{-1}$) over the southeastern slopes of the added ridge, which is close to the location of the convergence line. This

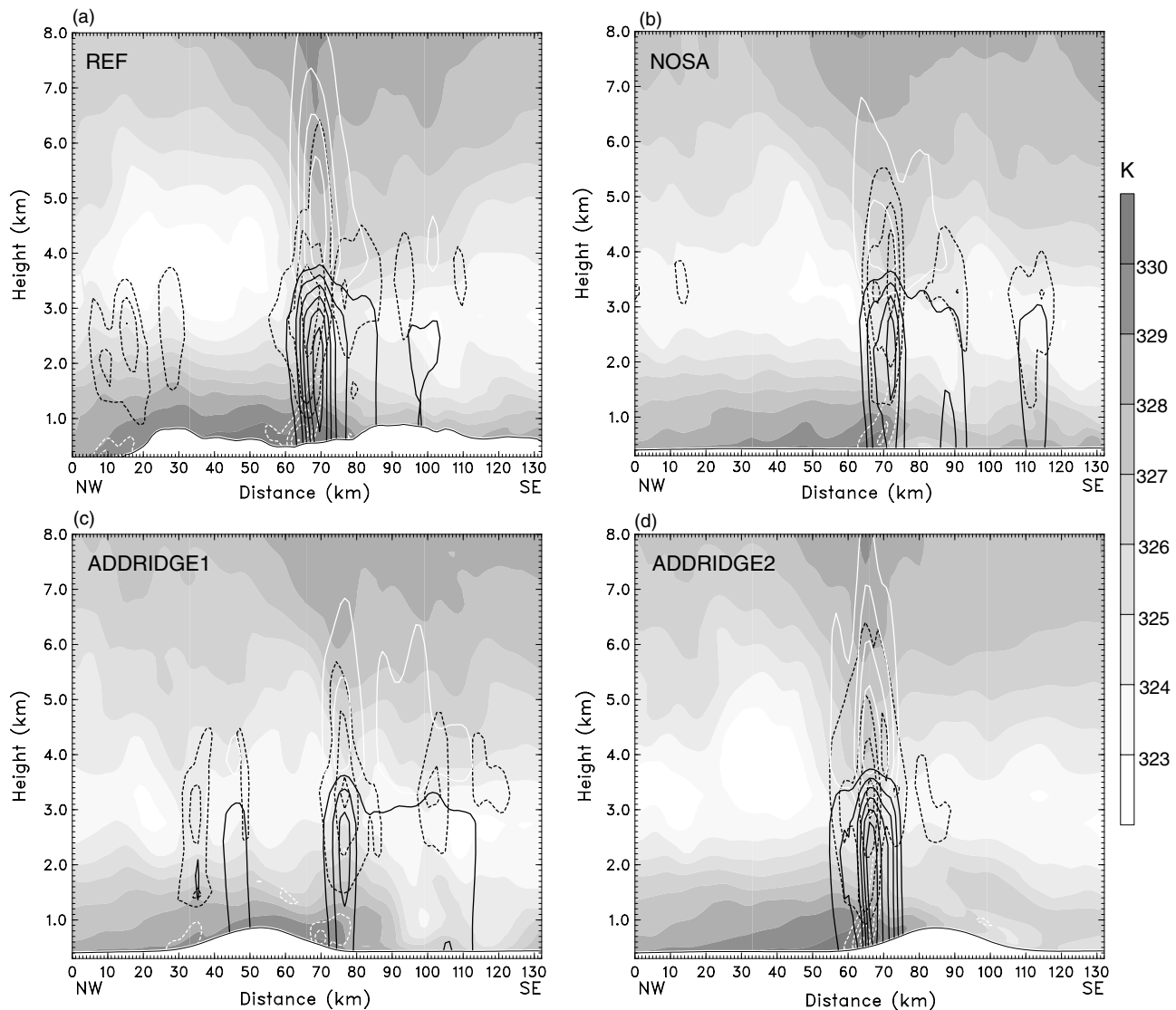


Figure 9. As Figure 8, but showing equivalent potential temperature (shading, K), horizontal wind convergence (white dashed contours with $40 \times 10^{-5} \text{ s}^{-1}$ increments, no zero contour), rain mixing ratio (black solid contours with 0.2 g kg^{-1} increments), cloud water (black dashed lines with 0.1 g kg^{-1} increments), and graupel mixing ratio (white solid contours with 0.4 g kg^{-1} increments).

stabilisation is confirmed by larger squares of both the dry and moist Brunt–Väisälä frequencies (not shown). The updraught magnitude of $\sim 0.8 \text{ m s}^{-1}$ (Figure 8(c)), which is smaller than in the REF and NOSA cases, indicates reduced deep-convective activity. Compared to the REF simulation, Figures 8(c) and 9(c) show similar values of CAPE ($\sim 300 \text{ J kg}^{-1}$) and θ_e , but a reduced low-level convergence. The delaying or weakening of deep convection due to atmospheric lids, regions of high CIN, and also their impact on the transition from shallow to deep convection has been shown in several previous studies (e.g. Morcrette *et al.*, 2007; Bennett *et al.*, 2008). Here, similar to these studies, a billow of increased static stability over the leeward slopes hinders the formation of strong convection. This is a consequence of subsidence due to downslope winds at the leeside of the ridge. The latter results from the cross-ridge inflow into the convergence line and might increase the vertical advection of potential temperature, which favours the formation of capping inversions. This simulation demonstrates that the presence of a ridge outside (but close to) the convergence line does not affect the primary region of convective updraughts in the convergence

line, but disorganises and scatters the banded structure by decreasing the continuity of convective initiation in the convergence line. This explains the decrease of precipitation in band A in the NOBF run, which placed the convergence line partially to the southeast of the SA. The simulation also reveals that a secondary mechanism for convective initiation is given by orographic lifting over the added idealised ridge. These findings suggest that the SA in the REF run, which is located underneath the convergence line or slightly to its south, does not disrupt the banded structure of the cells as much as the ADDRIDGE1 simulation, because in REF the location of secondary and primary trigger mechanism act in phase.

4.2.4. Additional idealised ridge 2

Within this experiment the artificial ridge from the previous simulation is adjusted to the position of the original SA and therefore shifted to the south by 40 km. Figure 3(g) shows the daily accumulated precipitation field of the ADDRIDGE2 run. A peak intensity is produced at the same location as in REF over the northwestern flank of the SA. Precipitation

band A produces ~ 20 mm more rainfall than in the ADDRIDGE1 simulation. Figure 6(e) shows that the low-level convergence line is located at the northwestern foothills of the ridge in the ADDRIDGE2 simulation at 1630 UTC on 21 August 2005. Thus, in contrast to ADDRIDGE1, convective initiation occurs above the northwestern flank and not to the southeast of the ridge. Furthermore, here the precipitation band is not affected by the subsiding inflow into the convergence line, which caused stabilisation in the ADDRIDGE1 run. The uniform convergence line to the northwest of the ridge (Figure 6(e)) causes an elongated precipitation band. The length of the band and its continuity agree very well with the REF run (Figure 6(a)).

The averaged vertical cross-section in Figure 8(d) reveals that CIN at the position of the low-level convergence is nearly half as large ($\sim 12 \text{ J kg}^{-1}$) as in the ADDRIDGE1 run. The maximum averaged vertical velocity is larger ($\sim 1.2 \text{ m s}^{-1}$) and the mean updraught starts closer to the ground. Furthermore, Figure 9(d) exhibits a stronger low-level convergence than in ADDRIDGE1 located right over the northwestern slope of the idealised ridge. CAPE and θ_e values are of comparable magnitude to ADDRIDGE1. Convective precipitation is not generated upstream of the convergence line, as the locations of the orographic triggering mechanism and the primary mechanism for convective initiation are merged above the northwestern slopes of the mountain. Note that, similar to the previous ADDRIDGE1 run in this simulation, convective inhibition is enhanced at the leeside of the ridge, but the magnitudes are significantly smaller than in the ADDRIDGE1 run, since the cross-ridge flow is weaker. This indicates that the strong stabilisation in ADDRIDGE1 results from an increased positive potential temperature advection at the southeastern slope of the ridge. Additionally, the ADDRIDGE2 simulation suggests that the precipitation in band A is enhanced only if the primary and secondary trigger mechanisms work in phase, i.e. the convergence line is centred above or slightly to the northwest of the ridgeline. To our knowledge, such topographic impacts on pre-existing convective features have not yet been studied explicitly. Previous literature on the modification of existing systems can only be found for, e.g. cyclone tracks (Lin *et al.*, 2005) or cold fronts (Steinacker, 1984). The observed modulation of pre-existing convection adds valuable information to the well-founded concept of orographic precipitation (e.g. Smith, 1979; Roe, 2005).

4.2.5. Flattened Alps

The daily accumulated precipitation field for the NOALPS simulation is shown in Figure 3(h). The spatial distribution still reveals some banded patterns, especially over the former SA region and over eastern Switzerland, but the intensity of the precipitation band over the SA and the precipitation maximum over central Switzerland are decreased by 50 mm with respect to the REF run. Horizontal precipitation gradients are smaller than in REF and rainfall reaches beyond the southern parts of Switzerland in the NOALPS run. Convective cells are continuously aligned and initiated by strictly confined convergence lines (Figure 6(f)). In contrast to the REF run, convection is restricted to areas of low-level convergence, since the orographic secondary trigger mechanism is missing here. Figure 6(f) shows precipitation band B, which is here located further to the north, while band A is located further to the south and is aligned

north–south (rather than southwest–northeast as in REF). Band A is not located over the SA region at 1630 UTC, but the convergence line is situated over eastern Switzerland with undisturbed northerly flow to its west and uniform northeasterly flow to its east. A comparison with the REF run shows a modified location of the cyclone itself in this experiment. The core of the cyclone is located further to the north and its pressure is slightly lower (not shown) than in the REF run, which contributes to a displacement of the convergence lines. After 1700 UTC, precipitation band A is located over southwestern Germany, where again a banded precipitation peak is generated (Figure 3(h)). The NOALPS run shows that, even without orographic forcing, convective precipitation bands are formed within lines of enhanced convergence. The latter are inherently embedded in the large-scale synoptic flow.

Here we would also like to mention that a further ‘dry’ sensitivity simulation without parametrisations of microphysical processes was conducted in order to address the question of whether the convergence lines were formed by the convectively induced circulation or whether existing convergence lines served as trigger mechanism for convection. Our ‘dry’ simulation revealed increased convergence within two flow-parallel aligned lines over southwestern Germany (not shown), although moist convection is missing. Maximum convergence reached up to almost $150 \times 10^{-5} \text{ s}^{-1}$ in both lines. Obviously, the generated convergence lines are not a consequence of the dynamics induced by the moist convection, but convection is triggered in a banded manner within the convergence lines, which appear to be associated with the synoptic configuration.

5. Summary and conclusions

Observations and numerical simulations of a convective period during an early stage of the Alpine heavy precipitation event in August 2005 have been presented in this article. The observational data consisted of a dense set of daily rain-gauge measurements, the CERAD radar composite, and vertical profiles from rawinsondes. The synoptic situation was characterised by a slowly eastward propagating cyclone located to the south of the Alps during the afternoon of 21 August 2005. The ECMWF operational analysis and the observed soundings showed a strong northeasterly low-level jet that transported large amounts of moisture towards the northern Alpine slopes. Conditional instability together with low-level directional shear and unidirectional shear above have been identified. Observations revealed two convective bands over southern Germany that enhanced the precipitation locally. Both bands were aligned from northeast to southwest and were initially located downstream of the BF. One band was subsequently situated further downstream above the northwestern slope of the flow-parallel aligned SA, while the other one remained closer to the BF.

In order to identify the trigger mechanisms of the convective bands and to study the topographic influence on their alignment, a reference simulation and further sensitivity simulations with selectively modified topography have been conducted using the WRF model. The reference run reproduced the synoptic situation and the accumulated precipitation field very well and captured the characteristics of the advected airmass. Despite discrepancies in the timing

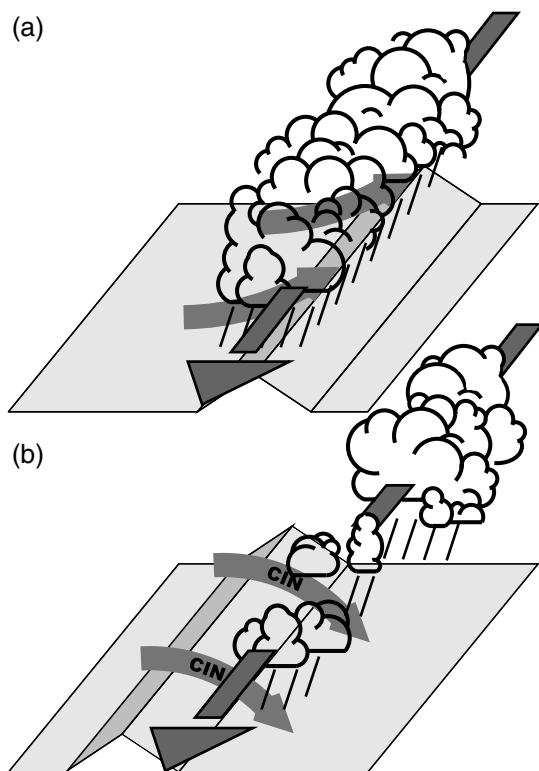


Figure 10. Schematic illustration of the interaction of a pre-existing convergence line, involving a pre-existing convective precipitation band, with a flow-parallel aligned mountain ridge. The position and advection of the convergence line/precipitation band is indicated by the dark arrow. (a) Enhancement and (b) suppression of the band's continuity and intensity occur if it is located (a) upstream and (b) downstream of the crestline with respect to the cross-barrier inflow (grey curved arrows) into the convergence line. In (b), convective inhibition results from stabilising descending inflow.

and exact locations of the convective bands, a qualitative agreement with the surface measurements and operational radars was achieved.

Our findings from a reference and several sensitivity experiments can be summarised as following:

- The triggering and alignment of convective cells over the low-mountain terrain in southern Germany is primarily determined by two synoptically forced low-level convergence lines.
- Neither the BF nor the SA play a significant role in determining the location of the convective precipitation bands, since convective cells would have been triggered and aligned without orographic forcing due to the presence of the above-mentioned primary mechanism for initiation.
- Although low-level convergence is sufficient to trigger the northern convective precipitation band over southwestern Germany, the intensity of this pre-existing band is enhanced by orographic lifting over the flow-parallel aligned SA.

From simulations with idealised flow-parallel aligned ridges, we conclude that the pre-existing banded structure of the convective cells is only supported if the primary trigger mechanism works in phase with the secondary orographic mechanism, i.e. the convergence line is situated upstream (or above) the ridge with respect to the cross-ridge inflow (as illustrated in Figure 10(a)). The continuity and intensity of the pre-existing precipitation band is

weakened and convective updraughts become disorganised if the convergence line is located not above the mountain ridge, but slightly further downstream (Figure 10(b)). The cross-barrier low-level inflow into the convergence line stabilises the atmosphere and hampers the development of a continuous convective precipitation band.

The presence of both small-scale and large-scale mechanisms for convective initiation illustrates the need for accurate numerical representations of boundary-layer processes (associated with small-scale topography) and synoptic-scale processes to predict intense and localised convective rainbands.

Acknowledgements

Rain-gauge data were provided by the national weather services ZAMG, DWD, MeteoSwiss, and by the Austrian Hydrological Service HZB. Thanks to all weather services contributing to the CERAD product, especially to Kurt Zimmermann (ZAMG). This work was supported by the Austrian Ministry of Science BMWF as part of the UniInfrastrukturprogramm of the Forschungsplattform Scientific Computing at LFU Innsbruck. The Central IT Services (ZID) as well as the High-Performance-Computing (HPC) Consortium of the University of Innsbruck are acknowledged for access to their Linux Computer Clusters.

References

- Bennett LJ, Blyth AM, Browning KA, Norton AG. 2008. Observations of the development of convection through a series of stable layers during the Convective Storm Initiation Project. *Q. J. R. Meteorol. Soc.* **134**: 2079–2091.
- Colle BA. 2004. Sensitivity of orographic precipitation to changing ambient conditions and terrain geometries: An idealized modeling perspective. *J. Atmos. Sci.* **61**: 588–605.
- Colle BA, Lin Y, Medina S, Smull BF. 2008. Orographic modification of convection and flow kinematics by the Oregon coastal range and Cascades during IMPROVE-2. *Mon. Weather Rev.* **136**: 3894–3916.
- Cosma S, Richard E, Miniscloux F. 2002. The role of small-scale orographic features in the spatial distribution of precipitation. *Q. J. R. Meteorol. Soc.* **128**: 75–92.
- Crook NA, Tucker DF. 2005. Flow over heated terrain. Part I: Linear theory and idealized numerical simulations. *Mon. Weather Rev.* **133**: 2552–2564.
- Dudhia J. 1989. Numerical study of convection observed during the winter monsoon experiment using a mesoscale two-dimensional model. *J. Atmos. Sci.* **46**: 3077–3107.
- Durrán DR, Klemp JB. 1983. A compressible model for the simulation of moist mountain waves. *Mon. Weather Rev.* **111**: 2341–2351.
- Fuhrer O, Schär C. 2005. Embedded cellular convection in moist flow past topography. *J. Atmos. Sci.* **62**: 2810–2828.
- Fuhrer O, Schär C. 2007. Dynamics of orographically triggered banded convection in sheared moist orographic flows. *J. Atmos. Sci.* **64**: 3542–3561.
- Godart A, Anquetin S, Leblois E. 2009. Rainfall regimes associated with banded convection in the Cévennes-Vivarais area. *Meteorol. Atmos. Phys.* **103**: 25–34.
- Hohenegger C, Walser A, Langhans W, Schär C. 2008. Cloud-resolving ensemble simulations of the August 2005 Alpine flood. *Q. J. R. Meteorol. Soc.* **134**: 889–904.
- Hong S-Y, Lim J-OJ. 2006. The WRF single-moment 6-class microphysics scheme (WSM6). *J. Korean Meteorol. Soc.* **42**: 129–151.
- Hong S-Y, Noh Y, Dudhia J. 2006. A new vertical diffusion package with an explicit treatment of entrainment processes. *Mon. Weather Rev.* **134**: 2318–2341.
- Jiang Q. 2003. Moist dynamics and orographic precipitation. *Tellus A* **55**: 301–316.
- Kain JS. 2004. The Kain–Fritsch convective parameterization: An update. *J. Appl. Meteorol.* **43**: 170–181.

- Kirshbaum DJ, Durran DR. 2004. Factors governing cellular convection in orographic precipitation. *J. Atmos. Sci.* **61**: 682–698.
- Kirshbaum DJ, Durran DR. 2005a. Observations and modeling of banded orographic convection. *J. Atmos. Sci.* **62**: 1463–1479.
- Kirshbaum DJ, Durran DR. 2005b. Atmospheric factors governing banded orographic convection. *J. Atmos. Sci.* **62**: 3758–3774.
- Kirshbaum DJ, Bryan GH, Rotunno R. 2007. The triggering of orographic rainbands by small-scale topography. *J. Atmos. Sci.* **64**: 1530–1549.
- Langhans W. 2008. 'Cloud-resolving simulations of the August 2005 Alpine flood: The sensitivity to microphysics parameterizations'. Master's thesis, University of Innsbruck: Austria.
- Lin Y-L, Chen S-Y, Hill CM, Huang C-Y. 2005. Control parameters for the influence of a mesoscale mountain range on cyclone track continuity and deflection. *J. Atmos. Sci.* **62**: 1849–1866.
- MeteoSchweiz. 2006a. *Starkniederschlagsereignis August 2005*. Arbeitsbericht 211, MeteoSchweiz: Zurich. Available online at <http://www.meteoschweiz.admin.ch>
- MeteoSchweiz. 2006b. *Eine Länder übergreifende Niederschlags-Analyse zum August-Hochwasser 2005: Ergänzung zu Arbeitsbericht 211*. Arbeitsbericht 213, MeteoSchweiz: Zurich. Available online at <http://www.meteoschweiz.admin.ch>
- Mlawer EJ, Taubmann SJ, Brown PD, Iacono MJ, Clough SA. 1997. Radiative transfer for inhomogeneous atmosphere: RRTM, a validated correlated-k model for the longwave. *J. Geophys. Res.* **102**: 16663–16682.
- Morcrette CJ, Lean H, Browning KA, Nicol J, Roberts N, Clark PA, Russell A, Blyth AM. 2007. Combination of mesoscale and synoptic mechanisms for triggering an isolated thunderstorm: Observational case-study of CSIP IOP 1. *Mon. Weather Rev.* **135**: 3728–3749.
- Randeu WL, Köck KF, Leitner T. 1996. 'Realisation of the Central European Weather Radar Network (CERAD)'. Final report, Technical University: Graz, Austria.
- Roe GH. 2005. Orographic precipitation. *Annu. Rev. Earth Planet. Sci.* **33**: 645–671.
- Rotunno R, Ferretti R. 2001. Mechanisms of intense Alpine rainfall. *J. Atmos. Sci.* **58**: 1732–1749.
- Schneider M, Schär C. 2000. Idealized numerical experiments of Alpine flow regimes and southside precipitation events. *Meteorol. Atmos. Phys.* **72**: 233–250.
- Schumacher RS, Schultz DM, Knox JA. 2010. Convective snowbands downstream of the Rocky Mountains in an environment with conditional, dry symmetric, and inertial instabilities. *Mon. Weather Rev.* **138**: 4416–4438.
- Skamarock WC, Weisman ML. 2009. The impact of positive-definite moisture transport on NWP precipitation forecasts. *Mon. Weather Rev.* **137**: 488–494.
- Skamarock WC, Klemp JB, Dudhia J, Gill DO, Barker DM, Wang W, Powers JG. 2005. 'A description of the Advanced Research WRF Version 2'. Technical note TN-468+STR. National Center for Atmospheric Research: Boulder, Colorado, USA.
- Smith RB. 1979. The influence of mountains on the atmosphere. *Adv. Geophys.* **27**: 87–230.
- Steinacker R. 1984. Airmass and frontal movement around the Alps. *Riv. Meteorol. Aeronaut.* **44**: 85–93.
- Tucker DF, Crook NA. 2005. Flow over heated terrain. Part II: Generation of convective precipitation. *Mon. Weather Rev.* **133**: 2565–2582.
- Yoshizaki M, Kato T, Tanaka Y, Takayama H, Shoji Y, Seko H, Arao K, Manabe K. 2000. Analytical and numerical study of the 26 June 1998 orographic rainband observed in Western Kyushu, Japan. *J. Meteorol. Soc. Japan* **78**: 835–856.
- Zängl G. 2004. The sensitivity of simulated orographic precipitation to model components other than cloud microphysics. *Q. J. R. Meteorol. Soc.* **130**: 1857–1875.
- Zängl G. 2007a. An adaptive vertical coordinate formulation for a non-hydrostatic model with flux-form equations. *Mon. Weather Rev.* **135**: 228–239.
- Zängl G. 2007b. Interaction between dynamics and cloud microphysics in orographic precipitation enhancement: A high-resolution modeling study of two north-Alpine heavy precipitation events. *Mon. Weather Rev.* **135**: 2817–2840.
- Zängl G. 2007c. To what extent does increased model resolution improve simulated precipitation fields? A case study of two north-Alpine heavy rainfall events. *Meteorol. Z.* **16**: 571–580.